



# Chromatin mechanics dictates subdiffusion and coarsening dynamics of embedded condensates

Daniel S. W. Lee <sup>1,2,3</sup>, Ned S. Wingreen <sup>1,3</sup> and Clifford P. Brangwynne <sup>1,2,4</sup>

**DNA is organized into chromatin, a complex polymeric material that stores information and controls gene expression. An emerging mechanism for biological organization, particularly within the crowded nucleus, is biomolecular phase separation into condensed droplets of protein and nucleic acids. However, the way in which chromatin impacts the dynamics of phase separation and condensate formation is poorly understood. Here we utilize a powerful optogenetic strategy to examine the interplay of droplet coarsening with the surrounding viscoelastic chromatin network. We demonstrate that droplet growth dynamics are directly inhibited by the chromatin-dense environment, which gives rise to an anomalously slow coarsening exponent,  $\beta \approx 0.12$ , contrasting with the classical prediction of  $\beta = 1/3$ . Using scaling arguments and simulations, we show how this arrested growth can arise due to subdiffusion of individual condensates, predicting  $\beta \approx \alpha/3$ , where  $\alpha$  is the diffusive exponent. Tracking the fluctuating motion of condensates within chromatin reveals a subdiffusive exponent,  $\alpha \approx 0.5$ , which explains the anomalous coarsening behaviour and is also consistent with Rouse-like dynamics arising from the entangled chromatin. Our findings have implications for the biophysical regulation of the size and shape of biomolecular condensates and suggest that condensate emulsions can be used to probe the viscoelastic mechanical environment within living cells.**

Liquid–liquid phase separation (LLPS) has emerged as a common assembly mechanism within living cells<sup>1,2</sup>. LLPS drives the formation of a multitude of biomolecular condensates such as nucleoli<sup>3</sup>, stress granules<sup>4</sup> and P granules<sup>5</sup>. Phase separation of proteins typically relies on multivalent interactions, and many efforts have been made to understand the role of self-interactions via intrinsically disordered protein regions (IDRs)<sup>6</sup> and heterotypic interactions, often mediated by folded protein–protein interaction domains and oligomerized RNA (or other substrate) binding domains. The condensates that result from these interactions are multicomponent structures, which range from compositionally homogeneous liquid-like structures to multiphase liquids and kinetically arrested gel states<sup>7–9</sup>. Their structural features and material properties are thought to enable a diversity of functions, ranging from increasing reaction rates by concentrating reactants to inhibiting reactivity through sequestration, and even structurally rearranging their environment<sup>1,10</sup>.

Many phase-separated condensates appear to exhibit stable sizes dependent on cell type<sup>11,12</sup>. It is unclear how these sizes are maintained, because liquid compartments should not have an intrinsic size scale. Rather, given enough time, individual condensates should coalesce to form a single, large droplet. In general, following a full quench of the system (that is, after nucleation and depletion of the dilute phase), the mean droplet radius is expected to evolve as a power law with exponent  $\beta$ , such that  $\langle R \rangle \approx t^\beta$ , where  $\beta = 1/3$ . Two distinct processes identically predict this exponent: (1) Lifshitz–Slyozov–Wagner (LSW) theory describes growth by Ostwald ripening<sup>13</sup> and (2) Brownian motion–driven coalescence (BMC) describes how individual droplets collide and fuse<sup>14</sup>. Droplet growth obeying this 1/3 power law has been observed in a variety of biological systems, including lipid membranes<sup>15</sup>, *in vitro* protein droplets and nucleoli in *Caenorhabditis elegans* embryos<sup>16</sup>, but distinguishing between the two mechanisms is not always possible.

In addition to the ambiguity in distinguishing these two processes, our understanding of the physics governing condensate coarsening within living cells is further complicated by the strongly viscoelastic nature of the intracellular environment. Indeed, droplet movements and interactions are expected to be strongly impacted by their viscoelastic environment. A particularly striking example of this interplay is found in *Xenopus laevis* oocytes, whose nuclei contain hundreds of nucleoli that are strongly constrained by an F-actin scaffold that only relaxes on very long timescales, giving rise to a broad power-law distribution of nucleolar sizes<sup>3</sup>. Upon actin disruption, the nucleoli sediment under gravity and undergo large-scale coalescence into a single massive nucleolus<sup>17</sup>. In human cell lines, nucleoli exhibit liquid-like properties of formation and fusion, but vary in their shapes and sizes<sup>18</sup>. Interestingly, these size and shape variations are tied to nuclear processes such as transcription and chromatin condensation<sup>19</sup>, suggesting that active processes can influence the properties and distribution of phase-separated condensates. Taken together, these findings are consistent with the shapes and sizes of nuclear condensates being strongly influenced by their physical environment.

As well as nucleoli, the nucleus contains dozens of different types of condensate, including Cajal bodies, paraspeckles, promyelocytic leukemia (PML) bodies and nuclear speckles, each of which is intimately associated with the surrounding chromatin network. Chromatin is the active polymeric material into which DNA and its associated proteins assemble and is packed into the nucleus at dense volume fractions, with measurements ranging from 12 to 52%<sup>20</sup>. Chromatin can be considered a continuous material on the length scale of microscopically visible droplets. Electron microscopy images<sup>20</sup>, as well as experiments utilizing microinjected fluorescent dextrans<sup>21</sup>, both suggest an average chromatin pore size of less than 100 nm (ref. <sup>22</sup>), although chromatin exhibits substantial heterogeneity on micrometre length scales<sup>23</sup>. Micromanipulation of

<sup>1</sup>Lewis-Sigler Institute for Integrative Genomics, Princeton University, Princeton, NJ, USA. <sup>2</sup>Department of Chemical and Biological Engineering, Princeton University, Princeton, NJ, USA. <sup>3</sup>Department of Molecular Biology, Princeton University, Princeton, NJ, USA. <sup>4</sup>Howard Hughes Medical Institute, Princeton, NJ, USA. e-mail: [wingreen@princeton.edu](mailto:wingreen@princeton.edu); [cbrangwy@princeton.edu](mailto:cbrangwy@princeton.edu)

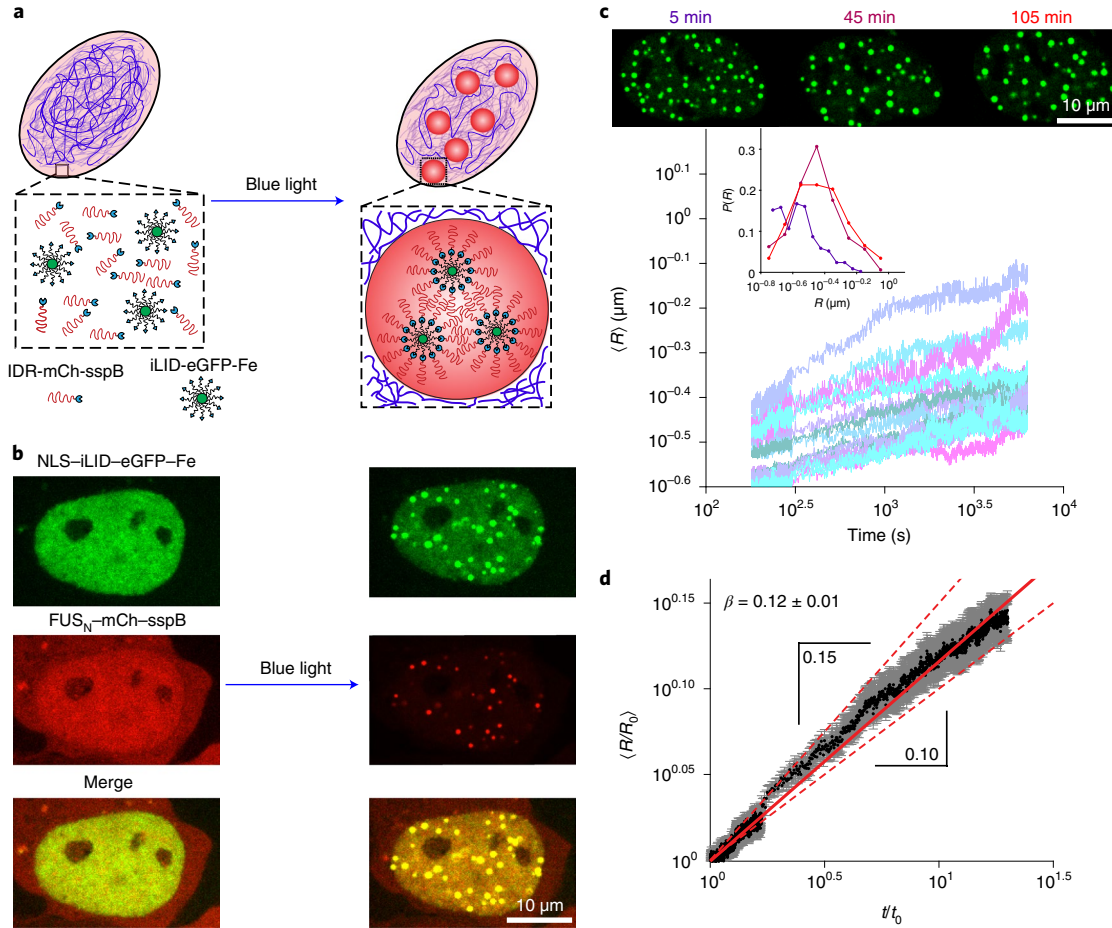


**Fig. 1 | Coarsening dynamics of light-activated protein condensates in living cells.** **a**, In the presence of blue light, the Corelet system recruits intrinsically disordered protein regions (IDRs; red) to the ferritin cores (green) to drive phase separation in the nuclei of living cells. **b**, Within seconds of exposure to blue light, droplets nucleate and grow. NLS, nuclear localization signal; eGFP, enhanced green fluorescent protein; mCh, mCherry. **c**, Top: images showing snapshots of FUS Corelet condensates at the indicated times. Bottom: average droplet radii for 18 cells calculated over 105 min and plotted starting 3 min after activation. Inset: the size distribution for eight cells with similar supersaturation (mean supersaturation of 1.3 with s.d. of 0.04) was taken at time points of 5, 45 and 105 min. **d**, The average radius of droplets per cell ( $\langle R/R_0 \rangle$ ) was plotted over time, after normalizing by the radius  $R_0$  of each droplet at the defined  $t_0$  of 3 min, revealing a power law with exponent of ~0.12 (solid red line). Error was propagated as s.e.m. The dashed red lines have slopes of 0.15 and 0.10, respectively.

extracted nuclei has also revealed that chromatin exhibits its own force response, independent of the nuclear lamina<sup>24</sup>, which has been the focus of most nuclear mechanics studies. Despite the clear functional importance of understanding the link between the dynamics of phase separation and the surrounding viscoelastic genetic material, very few studies have examined this connection.

Most studies have relied on simplified *in vitro* systems using purified components in an aqueous buffer. As a result, the impact of the cellular milieu on phase separation has generally remained unexplored, partly due to a lack of tools for interrogating phase separation in living cells<sup>25</sup>. However, recent advances have led to the development of optogenetic approaches, which utilize light to control intracellular phase separation through oligomerization of disordered and substrate binding domains<sup>7,22,26,27</sup>. Experiments using these systems have suggested that nuclear condensates preferentially form in relatively chromatin-poor regions and tend to exclude chromatin as they grow<sup>22</sup>. However, the physics governing the relationship between chromatin's material properties and the formation, mobility, growth and ultimate size distribution of embedded condensates remains unclear.

In this Article, we utilize the biomimetic Corelet system<sup>27</sup> to generate model IDR-based condensates and examine their coarsening

dynamics and interactions with chromatin in living cells. We demonstrate that coarsening in the nucleus is significantly slower than classical theory predicts, occurring primarily via coalescence, rather than via Ostwald ripening. Using particle-tracking experiments, we show that this slow coarsening results from strongly subdiffusive condensate motion, in quantitative agreement with a theoretical prediction relating the coarsening and diffusive exponents. The growth dynamics of embedded condensates are thus sensitively dependent on the viscoelasticity of the surrounding chromatin, representing a novel emulsion-based readout of the mechanical environment within living cells.

### Engineered condensates exhibit slow coarsening

To study interactions between proteinaceous condensates and chromatin, we utilized the two-component Corelet system<sup>27</sup> (Fig. 1) to control condensate formation in living cells. Corelets are based on a ferritin core composed of 24 subunits, each fused to an improved light-inducible dimer (iLID) domain, and a phase separation-driving IDR fused to stringent starvation protein B (sspB), iLID's optogenetic heterodimerization partner. Here, we used the IDR from the fused in sarcoma (FUS) protein, a member of the FET family of transcription factors<sup>28</sup>. We expressed these

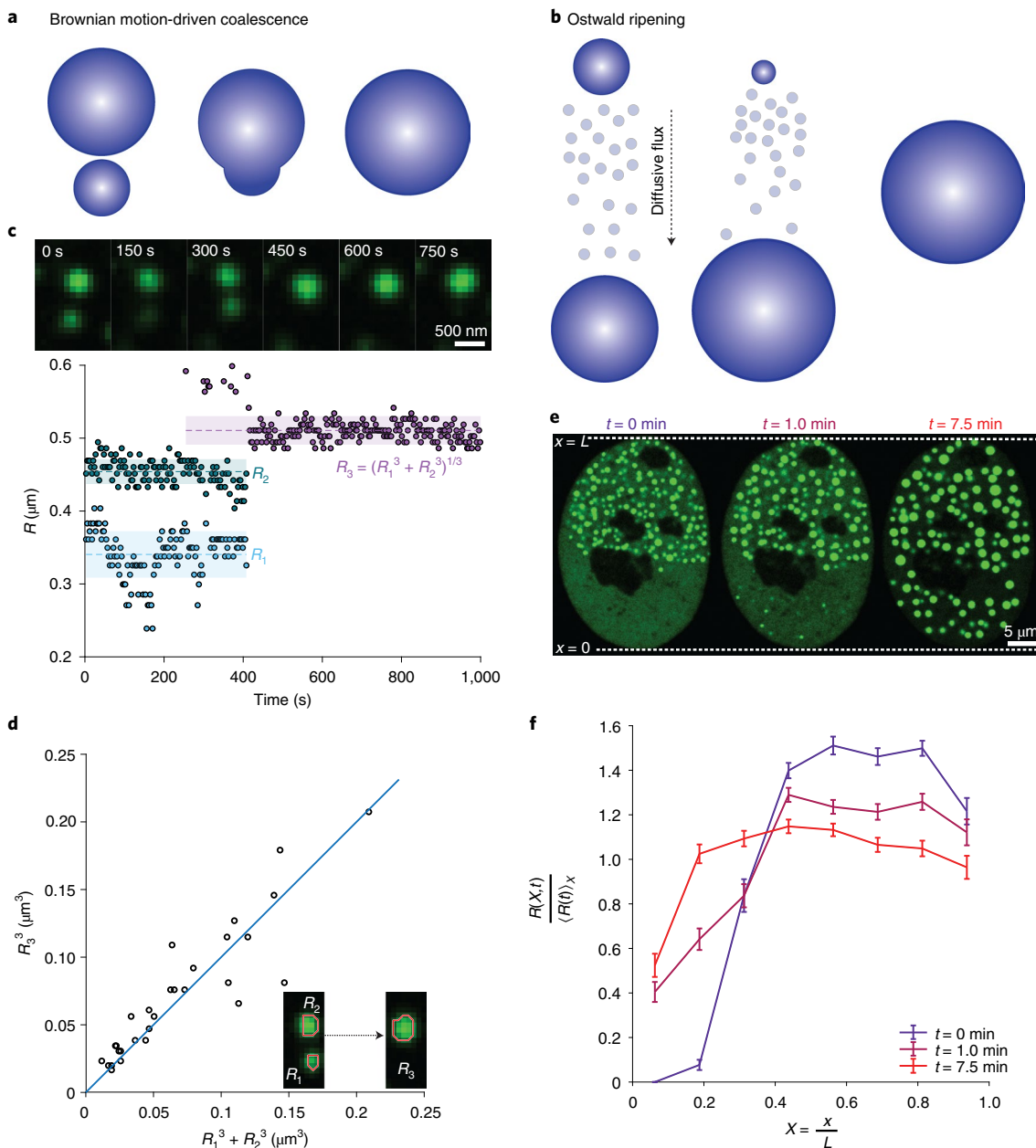


**Fig. 2 |** Droplet growth is dominated by coalescence. **a,b**, Emulsions generally coarsen by Ostwald ripening (**b**) or by mergers (**a**), respectively characterized by continuous and discrete growth. **c**, Example plot with select corresponding images, showing condensates are stable over long timescales, remaining the same size for minutes and then coming into contact (cyan and green points), before merging and settling at a stable size consistent with volume conservation (the dashed magenta line shows the predicted conserved volume of the final droplet and uncertainty of prediction is propagated from standard errors of the time-averaged means of the original two droplets). **d**, Volume conservation accounts for size changes over many collisions ( $n=29$ ). **e**, Gradient activations were used to generate polydisperse droplets. Following 30 s of activation with an intensity gradient of blue light, droplets formed primarily on the high-intensity side of the nucleus. After switching to global activation, new smaller droplets nucleated and grew on the other side of the nucleus. **f**, Quantification of the experiment described in **e** over 10 cells. Droplets were segmented and binned by location along the axis of the nucleus. Droplet size was normalized for each cell and averaged over cells. Error bars represent s.e.m.

constructs in human osteosarcoma (U2OS) cells, which contain nuclei typical of mammalian cells and yet are experimentally tractable, particularly for microscopy studies. Consistent with previous work<sup>27</sup>, upon blue-light activation, iLID and sspB bind, resulting in oligomerized IDR assemblies that phase-separate above a threshold of concentration and valence (degree of oligomerization). These model phase-separated nuclear condensates are visible within seconds of blue-light activation, providing a powerful platform for spatially and temporally interrogating the

impact of the viscoelastic environment on their dynamic coarsening behaviour.

We first sought to characterize droplet coarsening in live nuclei by activating cells and measuring Corelet droplets over the course of 105 min. At very early times, coarsening could be convoluted with nucleation and growth, initially driven by the supersaturated dilute phase, with an early-stage growth exponent predicted to be  $\frac{1}{2}$  (ref. <sup>29</sup>). We found that the dilute-phase intensity rapidly decreased and began stabilizing after  $\sim 3$  min of activation. A slow subsequent

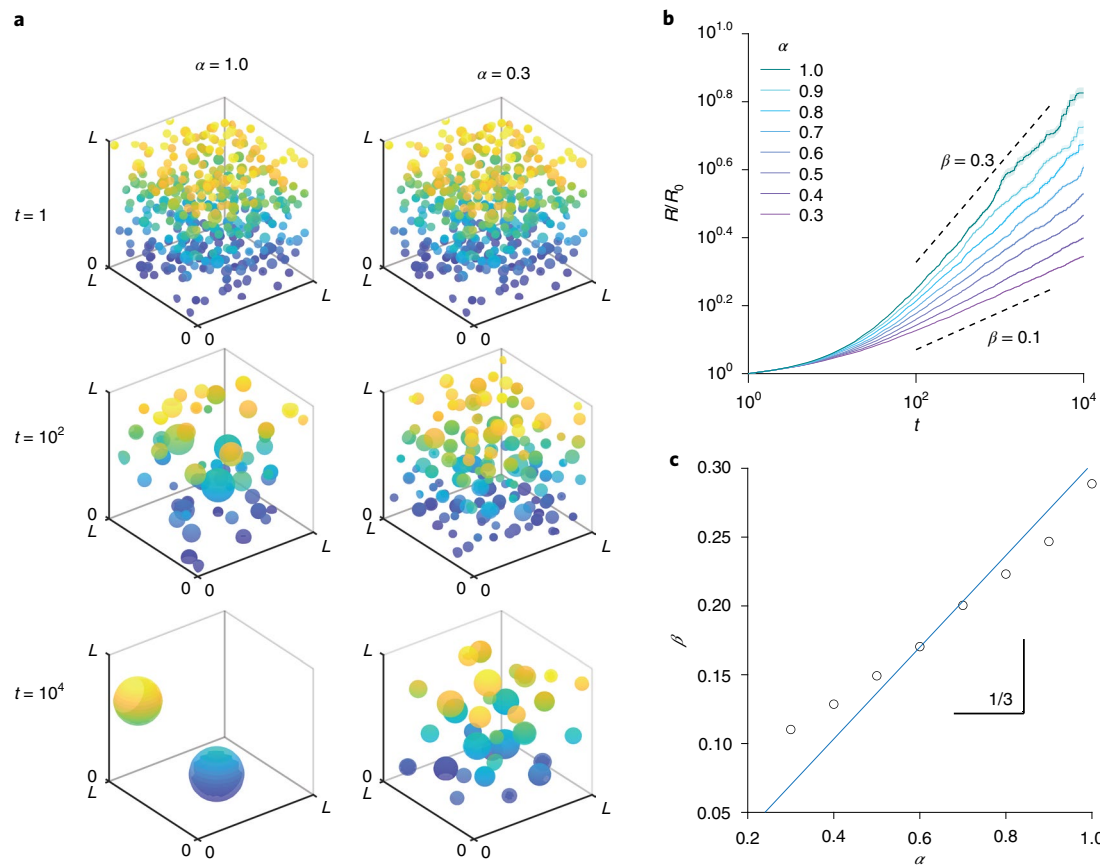


**Fig. 3 | Simulations quantitatively demonstrate the scaling relation between the diffusive exponent and the coarsening exponent.** **a**, A total of 500 droplets were placed in a three-dimensional box at a volume fraction of 0.05 and allowed to diffuse with a specified diffusive exponent  $\alpha$  and merge upon collision. **b**, Values of  $\alpha$  were chosen ranging from 0.3 to 1.0. For each of 20 replicates per condition, the average radius of the droplets was calculated, normalized to the average at  $t=0$ . The shaded regions indicate the s.e.m. **c**, For each simulation condition, the coarsening exponent  $\beta$  was calculated by fitting a power law starting at  $t=10^2$  and plotted against the input diffusive exponent  $\alpha$ .

linear decrease is probably due to photobleaching (Extended Data Fig. 1). We thus wait until after this transient dilute-phase equilibration and then probe the coarsening dynamics by determining the mean radius of droplets over time (Fig. 1c). Averaging over cells, we find a consistent power-law exponent of  $\beta=0.12 \pm 0.01$  (Fig. 1d). This low exponent is surprising, given that both Ostwald ripening and Brownian motion coalescence-dominated coarsening predict  $\beta=0.33$ , which is commonly observed in non-living systems<sup>15</sup>. Our results are not an artefact of the small size of droplets, as similar results were found by using integrated intensity as a proxy for size (Extended Data Fig. 2); moreover, extracted droplet sizes were robust to the choice of threshold (Extended Data Fig. 3). The observed heterogeneity across cells in initial droplet sizes is accounted for by variation in the expression of protein constituents, and individual fits on a per cell basis show that scaling behaviour follows a similar exponent, with more noise at low volume fraction (Extended Data Fig. 1).

#### Droplet coarsening is dominated by coalescence events

To elucidate the mechanism underpinning this anomalously slow growth, we investigated the relevance of two possible scenarios of droplet coarsening, Ostwald ripening (that is, LSW) and BMC (Fig. 2a,b). Although both mechanisms are driven by the minimization of surface energy, Ostwald ripening would occur via continuous growth/shrinkage of droplets, while a merger-dominated process would take place via discrete jumps in size associated with collision events. Consequently, we tracked pairs of droplets that merged,

finding that their sizes were stable for minutes before merger, at which point the resulting merged droplet attained the size predicted by volume conservation and remained that size for minutes in the absence of further collisions (Fig. 2c). This behaviour was consistent over 29 apparent mergers analysed across 18 cells, based on single bookending frames independently segmented before and after identified in-plane merger events (Fig. 2d), suggesting that growth over the entire bookended time interval ( $648 \pm 62$  s on average) was accounted for by coalescence.

These data are consistent with BMC-dominated coarsening, albeit with an anomalously low exponent. However, we reasoned that Ostwald ripening could also play a role in shrinkage and growth of unequal-sized droplets. To create a particularly polydisperse distribution, we activated nuclei with a low-intensity spatial gradient of blue light for 30 s, resulting in nuclei with droplets accumulated on one side and a local enrichment of protein in the dilute phase on the activated side, consistent with previously observed ‘diffusive capture’ of core molecules<sup>9</sup>. Switching to uniform blue-light stimulation resulted in fast equilibration of the dilute phase (<10 s, Extended Data Fig. 4) and therefore a uniform influx of newly activated molecules. Within minutes, we observed nucleation and growth of droplets on the previously unactivated side (Fig. 2e,f). We reasoned that if Ostwald ripening played an important role in the growth of our droplets, any small, newly nucleated droplets would quickly vanish because ripening would favour the preexisting ones, which are on the order of three- to fivefold larger in radius. However, we observed the opposite, finding that new droplets grew to a similar

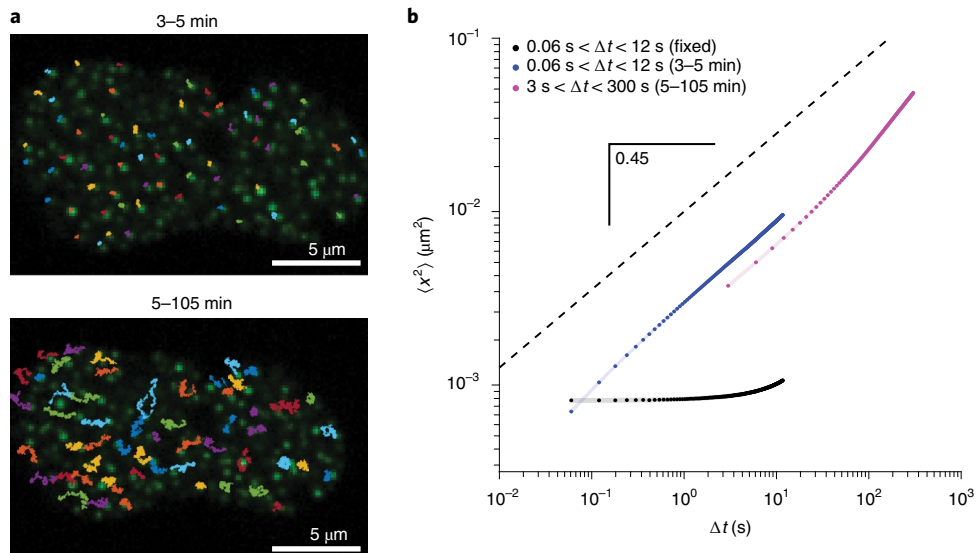


**Fig. 4 |** Droplets within the nucleus exhibit strongly subdiffusive motion. **a**, FUS Corelet condensates were tracked at a frame rate of 60 ms per frame for 2 min (starting 3 min after activation). They were then tracked for the following 100 min at 3 s per frame. Only droplets with continuously visible trajectories were tracked, with a minimum duration of 2 min in the short phase and 50 min in the long phase. **b**, MSDs for the short and long tracking phases are shown in blue and magenta, respectively, ensemble-averaged over 18 cells. Shaded regions indicate s.e.m. The magenta MSD follows a similar slope but demonstrates a nonlinear increase, probably due to stage and whole-nucleus drift. The noise floor (black data points) was estimated to be ~30 nm by applying the same tracking protocol on fixed cells, which exhibited similar long-term increases. Fitting the MSD of the fixed condensates gave an exponent of 0.08, which was used as a conservative estimate of the uncertainty for the diffusive exponent.

size as preexisting ones. Thus, we conclude that late-stage growth of our droplets is primarily driven by droplet coalescence events.

#### Coarsening exponent is related to diffusive exponent

Having empirically concluded that the coarsening of droplets is primarily driven by coalescence, we sought to quantitatively explain the anomalously slow coarsening exponent. We therefore revisited scaling arguments from the literature<sup>15</sup>, which assume ordinary diffusion of droplets. More generally, the rate at which droplets collide should depend on their mean squared displacement (MSD)—that is,  $\langle x \rangle^2 \approx D_R \Delta t^\alpha$ —where  $\alpha$  is the diffusion exponent ( $\alpha=1$  for ordinary diffusion,  $\alpha<1$  for subdiffusive motion, for example in a viscoelastic environment). At fixed droplet volume fraction (that is, having reached a steady-state dilute-phase concentration), the typical spacing  $l$  between droplets is related to their typical radius  $R$  by  $l \approx R$ . Then, assuming that droplets collide over a timescale at which their MSD equals their typical spacing, that is  $\langle x \rangle^2 \approx l^2$ , and assuming a diffusion coefficient  $D_R \approx R^{-1}$  as in Stokes drag, we find that  $R(t) \approx t^{\alpha/3}$ , that is,  $\beta = \alpha/3$ , confirming our intuition that subdiffusing droplets should coarsen slowly. Note that, in the case of ordinary diffusion ( $\alpha=1$ ), we recover the expected  $\beta=1/3$ .

To examine the validity of this scaling argument, we performed simulations on the coarsening of subdiffusing droplets according to fractional Brownian motion (fBM) with a step size inversely proportional to droplet radius, that is  $D_R \approx R^{-1}$ . Unsurprisingly, the more subdiffusive the motion, the slower the coarsening of the droplet size distribution (Fig. 3a). The average droplet radius over time was calculated for each simulation (Fig. 3b). We found that  $\beta \approx 0.3\alpha$ , in good agreement with our scaling argument.

To quantitatively test the predicted relationship between the coarsening and diffusive exponents, that is  $\beta = \alpha/3$ , we performed particle tracking on individual droplets to characterize their motion. Droplets were tracked over two timescales, at a rate of 60 ms per frame for 2 min and later at a rate of 3 s per frame for 100 min (Fig. 4a). The plotted MSDs were calculated by first time-averaging

within trajectories and then ensemble-averaging over all droplets for multiple cells (Fig. 4b). Over long timescales (several minutes), we found that bulk translation of the nucleus appeared to increase the MSD, so the diffusive exponent was taken from the early times. We find that droplets do, in fact, exhibit subdiffusive motion: from a fit over lag times  $\Delta t$  ranging from 60 ms to 12 s, we obtain an exponent of approximately  $\alpha = 0.48 \pm 0.08$ . Given the scaling argument above, this would give rise to a coarsening exponent of  $\beta = \alpha/3 \approx 0.16 \pm 0.03$ , consistent with our measured value of  $\beta = 0.12 \pm 0.01$  (Fig. 1d).

#### Droplet subdiffusion is due to constraints from chromatin

Our simulations and scaling argument are consistent with the surprisingly small measured coarsening exponent  $\beta$  arising from subdiffusive droplet dynamics. Given that the nucleus contains a dense chromatin network, we reasoned that the subdiffusive droplet dynamics are a result of the surrounding chromatin. We therefore examined the physical interactions between the droplets and chromatin. To generate droplets of a size above the diffraction limit we applied a local light activation protocol. We illuminated (for 10 min) an ~2-μm-diameter circular region in cells expressing histone H2B-green fluorescent protein (GFP), a marker of bulk DNA density. Consistent with previous experiments using the related CasDrop system, we observed depletion of the DNA marker from the droplet, suggesting that chromatin is largely excluded from the droplets (Fig. 5a,b). We found that IDR from several transcriptionally relevant proteins, including those from heterogeneous nuclear ribonucleoprotein A (HNRNPA), TATA-box binding protein associated factor 15 (TAF15) and bromodomain-containing protein 4 (BRD4), show a similar chromatin-exclusion effect (Fig. 5c). Consistent with our quantitative measurements of droplet MSDs (Fig. 4), these large droplets moved relatively little over minutes of observation. Similarly, following global activation for well over an hour, smaller droplets remained distributed throughout the nucleus, with their spatial position changing very little (Fig. 1c) and no evidence of global chromatin rearrangement or phototoxicity (Extended Data

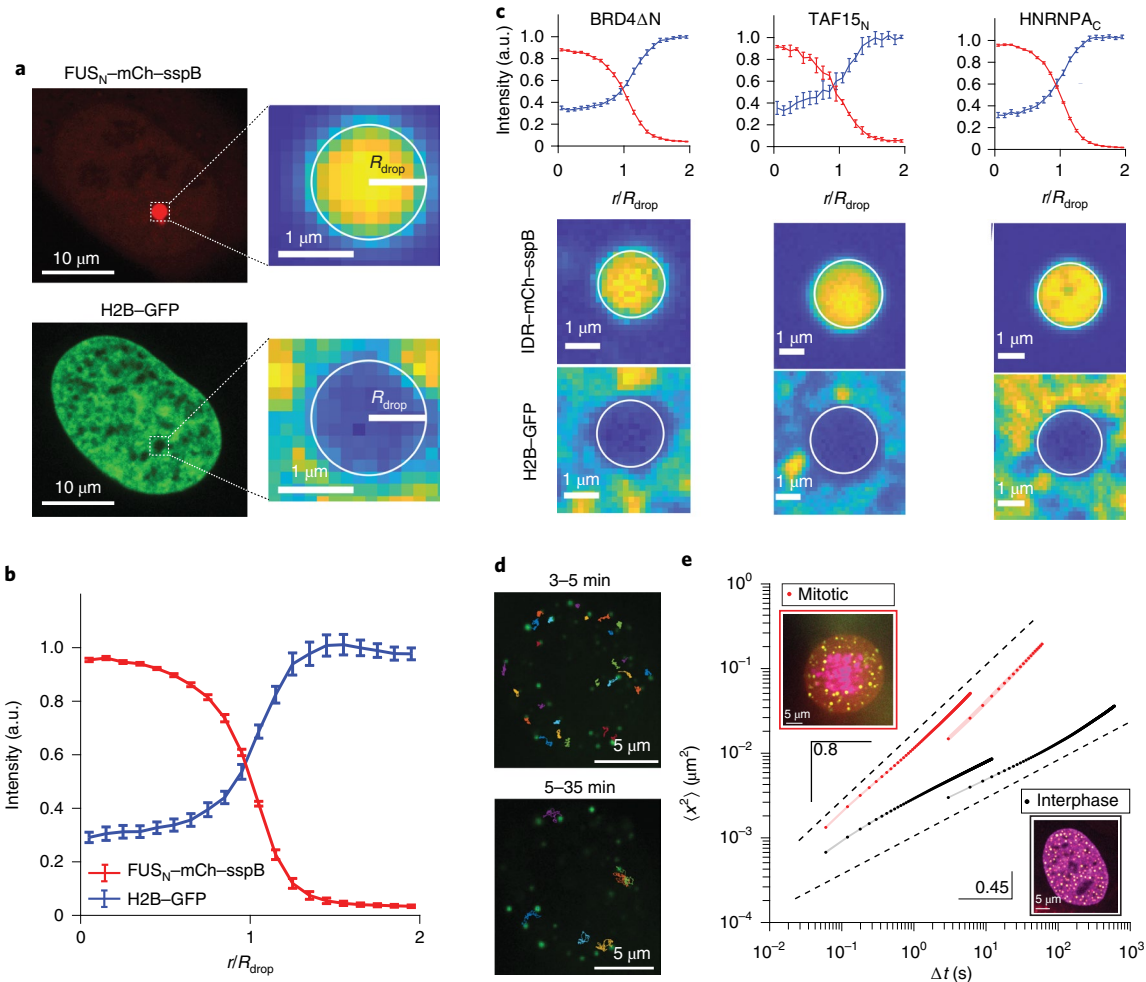


**Fig. 5 |** Droplets are constrained by chromatin. **a**, Droplets can be locally ‘written’ in specific locations by patterning blue-light stimulation. Co-labelling H2B-GFP demonstrates that droplets are generally associated with chromatin-sparse regions. **b**, Radially averaged intensity profiles of the H2B-GFP and droplet channels demonstrate that the chromatin is depleted within the droplet (averaged over 14 droplets). **c**, Identical analyses on droplets formed using IDR from BRD4, TAF15 and HNRNPA reveal similar exclusion of chromatin. Error bars show s.e.m. over 23, 8 and 23 droplets, respectively. **d**, FUS Corelet droplets were generated in mitotic cells (ranging from prometaphase to anaphase, identified by condensed chromosomes visible by H2B-miRFP expression) and tracked for time lags ranging from 60 ms to 200 s. **e**, MSDs were calculated for mitotic and interphase Corelet cells expressing H2B-miRFP (inset) and fit, revealing  $\alpha = 0.80 \pm 0.01$  (s.e.m. of linear fit) for mitotic cells compared with  $\alpha = 0.45 \pm 0.01$  for interphase H2B-miRFP control.

Figs. 5 and 6). We therefore surmised that droplets are constrained by the surrounding chromatin network.

To test directly whether the strongly subdiffusive dynamics indeed arise from constraints due to the surrounding viscoelastic chromatin network, we generated droplets in cells undergoing mitosis (Fig. 5d), in which chromatin-devoid regions surround the highly condensed mitotic chromosomes, visualized by an H2B-monomeric near-infrared fluorescent protein (miRFP) marker (Fig. 5e, insets). Tracking droplets generated in these mitotic cells revealed a considerably higher diffusive exponent  $\alpha = 0.80$  than the  $\alpha = 0.45$  in the interphase control (Fig. 5e), consistent with chromatin contributing strongly to the viscoelastic constraints on droplet motion (future studies will interrogate the possible additional impact of other nuclear components). We note that, in mitotic cells, droplets were generally few in number and moved out of focus quickly, precluding a quantitative examination of their coarsening dynamics. In all cases, we observed that the long- and short-timescale MSDs had a vertical offset, which can be attributed to the growth of the droplets in time—because droplets tracked for long periods of time have undergone more coarsening, they have a lower anomalous diffusion coefficient, which should depend on droplet size.

In principle, the diffusive exponent  $\alpha$  could also depend on droplet size, for example if droplet size were comparable to the chromatin mesh size, as observed in other biopolymer networks<sup>17,30</sup>. To examine this aspect further, we applied local activation, as described above, to generate droplets of greatly varying sizes (ranging from ~200 to 1,000 nm in radius; Fig. 6a, inset). Five-minute trajectories (with a frame rate of 60 ms per frame) were binned by droplet size and MSDs were ensemble-averaged and then fit (Fig. 6a). The diffusive exponent  $\alpha$  was  $\sim 0.5$  for all sizes (Fig. 6b), consistent with a chromatin mesh size below the radius of all interrogated droplets, in agreement with previous estimates<sup>22</sup>. These data also allow us to examine the dependence of the anomalous diffusive coefficient on droplet size (Fig. 6c). Interestingly, rather than exhibiting the usual Stokes dependence,  $D_R \approx R^{-1}$ , the best-fit power-law yields  $D_R \approx R^{-0.44 \pm 0.18}$  with a coefficient of determination of  $r^2 = 0.45$ , compared to  $r^2 = -0.26$  for a power-law slope of  $-1$ .

### The nuclear environment determines mechanisms of condensate coarsening

In this study, we sought to understand how the size distribution of intracellular protein condensates is impacted by their local

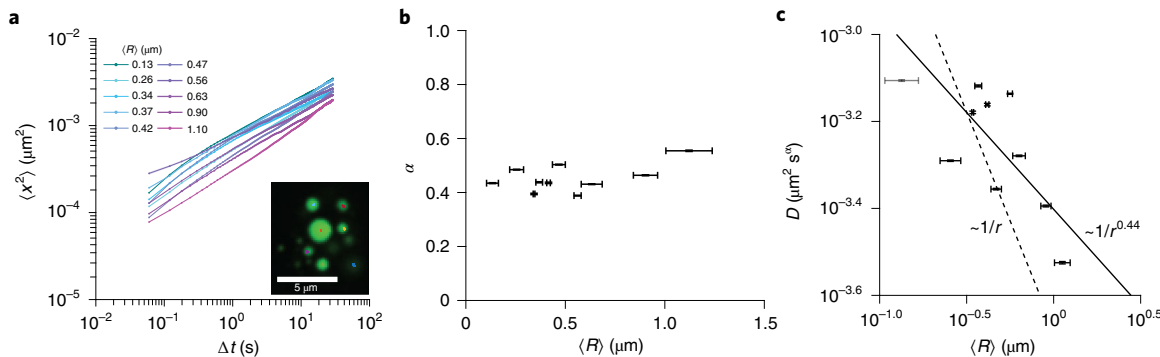


**Fig. 6 | Condensates as microrheological probes of the intracellular environment.** **a**, Local activation protocols generate size-selectable stable droplets (inset image). After initial stimulation, droplets were imaged for 5 min at 60 ms per frame and tracked for the entire video. Trajectories were binned by droplet size and time- and ensemble-averaged to produce an MSD for each size bin. The shaded region indicates s.e.m. **b**, Diffusive exponent versus droplet size. The horizontal error bars show the s.d. of droplet sizes in each bin, and the vertical error bars show the 95% confidence interval of the mean diffusive exponent from power-law fits. **c**, The anomalous diffusion coefficient,  $D$ , decreases with droplet size. The best-fit line (solid) is  $D \approx R^{-0.44 \pm 0.18}$  (standard error of the fit; coefficient of determination,  $r^2 = 0.45$ ). A  $D \approx R^{-1}$  reference line is also shown (dashed line;  $r^2 = -0.26$ ). The horizontal error bars show s.d. of droplet sizes in each bin, and the vertical error bars show the 95% confidence interval of the anomalous diffusion coefficient from power-law fits. For this fit, the smallest point ( $\langle R \rangle = 0.13 \pm 0.3 \mu\text{m}$ ; plotted in grey) was excluded because its s.d. overlapped with the diffraction limit.

mechanical environment. The two primary mechanisms for droplet coarsening are droplet coalescence (BMC) and Ostwald ripening (LSW), both of which predict a coarsening exponent of  $\beta = 1/3$ , significantly larger than our measurement of  $\beta = 0.12 \pm 0.01$ . Ostwald ripening is driven by surface tension, which for protein condensates is relatively small, on the order of  $10^{-7} \text{ N m}^{-1}$  (refs. <sup>18,31</sup>); these low values are consistent with the expected scaling  $\gamma \approx kT/\lambda^2$ , where  $\lambda$  is a characteristic (and for macromolecules a large) molecular length scale<sup>32</sup>. Considering parameters for FUS<sub>N</sub> Corelets<sup>27</sup>, we estimate that Ostwald ripening should drive droplet growth at a rate of  $\frac{dR}{dt} \approx 6 \times 10^{-7} \mu\text{m s}^{-1}$  for droplets with an initial radius of 300 nm (Supplementary Note). However, this estimate merely considers classical Ostwald ripening, which assumes concentration-independent monomer mobility<sup>33</sup>. Future studies will investigate whether Ostwald ripening is suppressed by additional physical mechanisms in these biological systems. By contrast, we estimate a slightly larger initial growth rate due to subdiffusive merger. Based on an average initial droplet spacing of  $1.3 \mu\text{m}$  (Supplementary Fig. 2) and our tracking data (Fig. 4b), we obtain an approximate growth rate of  $2 \times 10^{-6} \mu\text{m s}^{-1}$  (Supplementary Note). Calculating the average growth rate from our coarsening data (Fig. 1d), we obtain a larger average growth rate of  $2.4 \pm 0.3 \times 10^{-5} \mu\text{m s}^{-1}$ , but within an order of magnitude of this independent estimate.

Ostwald ripening is thus minimal, and instead the coarsening dynamics clearly appear to be dominated by droplet coalescence events, which we reasoned may be retarded by chromatin viscoelasticity. Indeed, from scaling arguments, and our simulation of a fractional Brownian walk, the classic  $\beta = 1/3$  prediction for BMC can be extended to subdiffusive random walks, yielding  $\beta = \alpha/3$ , where  $\alpha$  is the anomalous diffusion exponent. Consistent with this picture, tracking the motion of our model condensates reveals a high degree of subdiffusive constraint, with  $\alpha = 0.48$ . From this measurement, the  $\beta = \alpha/3$  prediction of  $\beta \approx 0.16 \pm 0.03$  is relatively close to the measured value of  $\beta = 0.12 \pm 0.01$ . The 30% deviation between these numbers could reflect additional physics that we do not take into account. For example, the dependence of the diffusive prefactor on droplet size may be non-Stokesian. However, our best fit yields  $D_R \approx R^{-0.5}$ , which invites a correction of the scaling argument to  $\beta = \alpha/2.5$  (which was confirmed in simulation, Extended Data Fig. 7), increasing the deviation from theory. Instead, the lower value of the ripening exponent  $\beta$  could be due to caging—on very long timescales, we anticipate that the MSD should saturate due to the

presence of boundaries (for example, heterochromatic domains), further slowing the merger process. This saturation of the MSD may take place on very long timescales, which were not captured here. We also note that we tracked condensates and considered them to be entirely independent, while local compressive stresses could cause droplets to slow down when in the vicinity of one another but still merge rapidly when the cavities they induce in the chromatin meet, explaining correlated motions observed in endogenous organelles immediately preceding merger<sup>19,32</sup>.

Previous work has examined how slow, viscoelastic relaxation of the dilute (solvent-rich) phase can kinetically stabilize an emulsion by suppressing droplet coalescence and Ostwald ripening<sup>34</sup>. However, within the nucleus of living cells, we demonstrate that subdiffusion of droplets can slow but not arrest the coalescence of droplets, which are still able to contact one another and merge quickly. Interestingly, while the strongly viscoelastic nature of the surrounding chromatin can retard droplet coalescence, it may also underlie our finding that droplet coalescence is dominant compared to Ostwald ripening. Although surface tension drives a preference for the growth of larger droplets, when embedded in a porous elastic matrix, smaller droplets result in smaller deformations and therefore potentially lower energetic costs, dependent on the relative magnitudes of the surface tension and matrix elasticity. It has also been shown that the spring constant of chromatin for micrometre-scale perturbations is  $\sim 10^{-3} \text{ N m}^{-1}$  (ref. <sup>24</sup>), four orders of magnitude larger than its surface tension<sup>18,31</sup>. Therefore, depending on the exact constitutive laws governing chromatin, droplet exclusion and the associated deformation of chromatin could actually stabilize smaller droplets, even in the presence of large ones. Similar observations of ‘inverse ripening’ have been made in synthetic systems of droplets embedded in strain-stiffening gels<sup>35,36</sup>.

### Condensates as probes of nuclear mechanics

The intimate link between droplet coarsening dynamics and chromatin viscoelasticity underscores the potential for utilizing these model condensates as passive microrheological probes. Nucleoli and other endogenous condensates have been proposed as probes in a similar fashion<sup>19</sup>, but their dynamics are confounded by essential biological processes, such as nucleation at specific sites and non-equilibrium activity<sup>18</sup>, and by their multicomponent nature<sup>37</sup>. By contrast, our engineered optogenetic droplets can be assembled from IDRs lacking folded interaction domains, and the resulting

probe (droplet) size can be controlled using local activation protocols. Within the nucleus, our optogenetic droplets report on the viscoelastic nature of the entangled chromatin matrix. We find strongly subdiffusive dynamics, with  $\alpha=0.48$  and  $D_R=R^{-0.44\pm0.18}$ , roughly consistent with the Rouse polymer model, which predicts  $\alpha=0.5$  and  $D_R=R^{-0.5}$ . The Rouse model describes the dynamics of a polymer of beads connected by springs<sup>38</sup> and has been used to describe subdiffusion in other biological systems, including individual chromosomal loci, for example, in *Escherichia coli* and *Caulobacter crescentus*<sup>39</sup> and telomeres<sup>40</sup>. Although these sites are tethered to the rest of the genome, we speculate that a droplet immersed in a viscoelastic gel and far above the mesh size should exhibit similar dynamics. Future studies will apply this technique to interrogate the mechanical properties of chromatin under varying perturbations.

Our findings also have implications for the assembly of endogenous condensates. Cajal bodies and nucleoli, associated with relatively chromatin-poor regions, have also been shown to exhibit subdiffusive dynamics, which, moreover, are sensitive to drug treatment (for example, ATP depletion and transcriptional inhibition<sup>41,42</sup>). Similarly, nuclear speckles display increased mobility as well as increased merger frequency upon transcriptional inhibition and subsequent chromatin condensation<sup>43</sup>. Thus, chromatin condensation and mechanics probably influence the sizes of endogenous biomolecular condensates. Future studies will investigate the roles of non-equilibrium biological processes and of specific interactions in the interplay between chromatin mechanics and phase separation.

### Online content

Any methods, additional references, Nature Research reporting summaries, source data, extended data, supplementary information, acknowledgements, peer review information; details of author contributions and competing interests; and statements of data and code availability are available at <https://doi.org/10.1038/s41567-020-01125-8>.

Received: 18 May 2020; Accepted: 16 November 2020;  
Published online: 11 January 2021

### References

- Shin, Y. & Brangwynne, C. P. Liquid phase condensation in cell physiology and disease. *Science* **357**, eaaf4382 (2017).
- Banani, S. F., Lee, H. O., Hyman, A. A. & Rosen, M. K. Biomolecular condensates: organizers of cellular biochemistry. *Nat. Rev. Mol. Cell Biol.* **18**, 285–298 (2017).
- Brangwynne, C. P., Mitchison, T. J. & Hyman, A. A. Active liquid-like behavior of nucleoli determines their size and shape in *Xenopus laevis* oocytes. *Proc. Natl Acad. Sci. USA* **108**, 4334–4339 (2011).
- Ivanov, P., Kedersha, N. & Anderson, P. Stress granules and processing bodies in translational control. *Cold Spring Harb. Perspect. Biol.* **11**, a032813 (2019).
- Brangwynne, C. P. et al. Germline P granules are liquid droplets that localize by controlled dissolution/condensation. *Science* **324**, 1729–1732 (2009).
- Brangwynne, C. P., Tompa, P. & Pappu, R. V. Polymer physics of intracellular phase transitions. *Nat. Phys.* **11**, 899–904 (2015).
- Sanders, D. W. et al. Competing protein–RNA interaction networks control multiphase intracellular organization. *Cell* **181**, 306–324.e28 (2020).
- Li, L. et al. Real-time imaging of Huntington aggregates diverting target search and gene transcription. *eLife* **5**, e17056 (2016).
- Patel, A. et al. A liquid-to-solid phase transition of the ALS protein FUS accelerated by disease mutation. *Cell* **162**, 1066–1077 (2015).
- Bergeron-Sandoval, L.-P. et al. Endocytosis caused by liquid–liquid phase separation of proteins. Preprint at *bioRxiv* <https://www.biorxiv.org/content/10.1101/145664v3> (2018).
- Brangwynne, C. P. Phase transitions and size scaling of membrane-less organelles. *J. Cell Biol.* **203**, 875–881 (2013).
- Weber, S. C. & Brangwynne, C. P. Inverse size scaling of the nucleolus by a concentration-dependent phase transition. *Curr. Biol.* **25**, 641–646 (2015).
- Lifshitz, I. M. & Slyozov, V. V. The kinetics of precipitation from supersaturated solid solutions. *J. Phys. Chem. Solids* **19**, 35–50 (1961).
- Siggia, E. D. Late stages of spinodal decomposition in binary mixtures. *Phys. Rev. A* **20**, 595–605 (1979).
- Stanich, C. A. et al. Coarsening dynamics of domains in lipid membranes. *Biophys. J.* **105**, 444–454 (2013).
- Berry, J., Weber, S. C., Vaidya, N., Haataja, M. & Brangwynne, C. P. RNA transcription modulates phase transition-driven nuclear body assembly. *Proc. Natl Acad. Sci. USA* **112**, E5237–E5245 (2015).
- Feric, M. & Brangwynne, C. P. A nuclear F-actin scaffold stabilizes ribonucleoprotein droplets against gravity in large cells. *Nat. Cell Biol.* **15**, 1253–1259 (2013).
- Caragine, C. M., Haley, S. C. & Zidovska, A. Surface fluctuations and coalescence of nucleolar droplets in the human cell nucleus. *Phys. Rev. Lett.* **121**, 148101 (2018).
- Caragine, C. M., Haley, S. C. & Zidovska, A. Nucleolar dynamics and interactions with nucleoplasm in living cells. *eLife* **8**, e47533 (2019).
- Ou, H. D. et al. ChromEMT: visualizing 3D chromatin structure and compaction in interphase and mitotic cells. *Science* **357**, eaag0025 (2017).
- Görisch, S. M., Wachsmuth, M., Tóth, K. F., Lichter, P. & Rippe, K. Histone acetylation increases chromatin accessibility. *J. Cell Sci.* **118**, 5825–5834 (2005).
- Shin, Y. et al. Liquid nuclear condensates mechanically sense and restructure the genome. *Cell* **175**, 1481–1491 (2018).
- Zidovska, A., Weitz, D. A. & Mitchison, T. J. Micron-scale coherence in interphase chromatin dynamics. *Proc. Natl Acad. Sci. USA* **110**, 15555–15560 (2013).
- Stephens, A. D., Banigan, E. J., Adam, S. A., Goldman, R. D. & Marko, J. F. Chromatin and lamin A determine two different mechanical response regimes of the cell nucleus. *Mol. Biol. Cell* **28**, 1984–1996 (2017).
- Bracha, D., Walls, M. T. & Brangwynne, C. P. Probing and engineering liquid-phase organelles. *Nat. Biotechnol.* **37**, 1435–1445 (2019).
- Shin, Y. et al. Spatiotemporal control of intracellular phase transitions using light-activated optodroplets. *Cell* **168**, 159–171 (2017).
- Bracha, D. et al. Mapping local and global liquid phase behavior in living cells using photo-oligomerizable seeds. *Cell* **175**, 1467–1480 (2018).
- Schwartz, J. C., Cech, T. R. & Parker, R. R. Biochemical properties and biological functions of FET proteins. *Annu. Rev. Biochem.* **84**, 355–379 (2015).
- Radke, L. & Voorhees, P. *Growth and Coarsening: Ripening in Material Processing, Engineering Materials and Processes* (Springer, 2002).
- Wong, I. Y. et al. Anomalous diffusion probes microstructure dynamics of entangled F-actin networks. *Phys. Rev. Lett.* **92**, 178101 (2004).
- Feric, M. et al. Coexisting liquid phases underlie nucleolar subcompartments. *Cell* **165**, 1686–1697 (2016).
- Aarts, D. G. A. L., Schmidt, M. & Lekkerkerker, H. N. W. Direct visual observation of thermal capillary waves. *Science* **304**, 847–850 (2004).
- Bray, A. J. & Emmott, C. L. Lifshitz–Slyozov scaling for late-stage coarsening with an order-parameter-dependent mobility. *Phys. Rev. B* **52**, R685 (1995).
- Tanaka, H. Viscoelastic phase separation. *J. Phys. Condens. Matter* **12**, R207 (2000).
- Rosowski, K. A. et al. Elastic ripening and inhibition of liquid–liquid phase separation. *Nat. Phys.* **16**, 422–425 (2020).
- Style, R. W. et al. Liquid–liquid phase separation in an elastic network. *Phys. Rev. X* **8**, 011028 (2018).
- Riback, J. A. et al. Composition-dependent thermodynamics of intracellular phase separation. *Nature* **581**, 209–214 (2020).
- Weber, S. C., Theriot, J. A. & Spakowitz, A. J. Subdiffusive motion of a polymer composed of subdiffusive monomers. *Phys. Rev. E* **82**, 011913 (2010).
- Weber, S. C., Spakowitz, A. J. & Theriot, J. A. Nonthermal ATP-dependent fluctuations contribute to the *in vivo* motion of chromosomal loci. *Proc. Natl Acad. Sci. USA* **109**, 7338–7343 (2012).
- Bronshtein, I. et al. Loss of lamin A function increases chromatin dynamics in the nuclear interior. *Nat. Commun.* **6**, 8044 (2015).
- Platani, M., Goldberg, I., Lamond, A. I. & Swedlow, J. R. Cajal body dynamics and association with chromatin are ATP-dependent. *Nat. Cell Biol.* **4**, 502–508 (2002).
- Görisch, S. M. et al. Nuclear body movement is determined by chromatin accessibility and dynamics. *Proc. Natl Acad. Sci. USA* **101**, 13221–13226 (2004).
- Kim, J., Han, K. Y., Khanna, N., Ha, T. & Belmont, A. S. Nuclear speckle fusion via long-range directional motion regulates speckle morphology after transcriptional inhibition. *J. Cell Sci.* **132**, jcs226563 (2019).

**Publisher's note** Springer Nature remains neutral with regard to jurisdictional claims in published maps and institutional affiliations.

© The Author(s), under exclusive licence to Springer Nature Limited 2021

## Methods

**Cell culture.** U2OS (a kind gift from the M. Groudine lab at the Fred Hutchinson Cancer Research Center) and Lenti-X 293T (Takara) cells were cultured in growth medium consisting of Dulbecco's modified Eagle's medium (GIBCO), 10% fetal bovine serum (Atlanta Biologicals) and 10 U ml<sup>-1</sup> penicillin-streptomycin (GIBCO), and incubated at 37°C and 5% CO<sub>2</sub> in a humidified incubator.

**Lentiviral transduction.** Lentivirus was produced by transfecting the transfer plasmid, pCMV-dR8.91 and pMD2.G (9:8:1, mass ratio) into Lenti-X cells grown to ~80% confluence in six-well plates using FuGENE HD transfection reagent (Promega) according to the manufacturer's protocol. A total of 3 µg of plasmid and 9 µl of transfection reagent were delivered into each well. After 60–72 h, supernatant containing viral particles was collected and filtered with a 0.45-µm filter (Pall Life Sciences). Supernatant was immediately used for transduction or aliquoted and stored at -80°C. U2OS cells were seeded at 10% confluence in 96-well plates and 20–200 µl of filtered viral supernatant was added to the cells. Medium containing virus was replaced with fresh growth medium 24 h post-infection. Infected cells were imaged no earlier than 72 h after infection.

**Cell line generation.** To generate a population of cells stably expressing H2B-miRFP670 or H2B-GFP, cells were infected in a six-well plate, transferred to a 60-mm plate, and finally sorted with a flow cytometer (BD Biosciences), with gating for single cells at intermediate to high levels of miRFP670 or GFP. The sorted cell line was then infected with viral supernatant as described above to express Corelet components. Gradient activation experiments were performed in the H2B-miRFP670 cell line so that the entire nucleus was visible at all times.

**Cell fixation.** Cells infected with lentivirus and plated on a 96-well plate as described above were placed on a 96-well-plate light-emitting diode (LED) array (Aamuza) for 15 min, after which medium was aspirated and 4% paraformaldehyde (Electron Microscopy Sciences, diluted in PBS) was added and the plate remained on the LED array for a further 15 min. Cells were then imaged and droplets tracked as otherwise described. MSDs were calculated and used to reflect systematic experimental error in the live-cell data.

**Microscopy.** All images were taken with a spinning-disk (Yokogawa CSU-X1) confocal microscope with a ×100 oil immersion Apo TIRF objective (NA 1.49) and an Andor DU-897 electron-multiplying charge-coupled device camera on a Nikon Eclipse Ti body. A 488 nm laser was used for imaging GFP and global activation, and a 561 nm laser for imaging mCherry. The imaging chamber was maintained at 37°C and 5% CO<sub>2</sub> (Oklab) with a 96-well plate adaptor. Local activation was performed by using a Mightex Polygon digital micromirror device to pattern blue light (485 nm) stimulation from a Lumencor SpectraX light engine using Nikon Elements software. Images were taken in a single central z plane for each nucleus using Perfect Focus to maintain the focal depth of the sample over time. We saw no evidence of phototoxicity, as the chromatin outside the droplets appeared unaffected following imaging (Extended Data Figs. 5 and 6).

**Image analysis. Image segmentation.** All images were analysed in Fiji (ImageJ 1.52p)<sup>44</sup> and MATLAB 2019b (Mathworks). Individual cells were cropped by hand and saved as tif files, which were analysed in MATLAB. Briefly, droplets were segmented in the GFP channel by using Otsu's algorithm to identify the nucleus in the first frame. An intensity threshold was defined as two standard deviations above the mean of the initial nuclear GFP intensity. This threshold was applied to all following frames to identify droplets, and regions of 4 pixels and smaller were discarded. Then, *regionprops* was used to identify individual domains and calculate their area. Radii were calculated by dividing the area by  $\pi$  and taking the square root. To calculate the volume fraction, the dilute phase of the nucleus was identified by applying a threshold at three standard deviations above the background concentration (characterized by imaging a sample with no fluorescence). In instances where no initial, pre-activation green channel was available (for example, local activation experiments), Otsu's method (*imbinarize* in MATLAB) was used to determine an intensity threshold for droplets. For gradient activation experiments, Otsu's method was used to segment nuclei in the miRFP channel, and again applied to pixels identified as being inside the nuclei to identify droplets on a per-frame basis. All results were validated by manual inspection.

**Particle tracking and registration.** To track particles, image registration was first performed to correct for rigid body motion using the StackReg plugin in Fiji. Subpixel tracking was then performed in TrackMate<sup>45</sup> using a Laplacian of Gaussians filter-based detector and a blob diameter of 500 nm (or an appropriate size for local activation experiments with large droplets), a threshold of 250. Trajectories were then constructed using the simple linear assignment problem

(LAP) tracking with max linking and gap-closing distances of 500 nm and no frame gap accepted. Only trajectories spanning the entire video (or in the case of the mitotic and 100-min videos, at least half the video) were accepted. Coordinates were then loaded into MATLAB to calculate MSDs and cross-correlations.

**Simulations.** Simulations were performed in MATLAB on the Della cluster (Princeton Research Computing). First, 500 droplets of identical radius (1 a.u.) were generated in three dimensions with periodic boundary conditions. Box size was based on the volume fraction, which was set to 5%. Overlapping droplets were then merged. Droplet merger was implemented by randomly selecting a pair of overlapping droplets and replacing them with one new droplet centred at their centre of mass. The size of the new droplet was determined by volume conservation of the original pair. This was iterated until no pairs of overlapping droplets remained. Then, for each droplet, a fractional Brownian motion trajectory with the appropriate  $\alpha$  was synthesized (*wfbm*) for the appropriate number of timesteps (generally set to 10<sup>4</sup>). The step size was set such that a droplet of radius 1 a.u. would diffuse an average of 1 a.u. in 3D per timestep. At each timepoint, each droplet proceeded one step along the synthesized trajectory, scaled by the inverse of the droplet size in the case of  $D_R \approx 1/R$ . Droplets were merged as previously described. Merged droplets 'inherited' the predetermined trajectory from one of their parent droplets (chosen arbitrarily), moving with the appropriate step size. This was repeated for the duration of the synthesized trajectories. The coarsening exponent  $\beta$  was obtained by fitting a power law starting at  $t = 10^2$ .

**Reporting Summary.** Further information on research design is available in the Nature Research Reporting Summary linked to this Article.

## Data availability

All data within this paper are available from C.P.B. upon reasonable request.

## Code availability

All code utilized in this paper is available from C.P.B. upon reasonable request.

## References

44. Schindelin, J. et al. Fiji: an open-source platform for biological-image analysis. *Nat. Methods* **9**, 676–682 (2012).
45. Tinevez, J.-Y. et al. TrackMate: an open and extensible platform for single-particle tracking. *Methods* **115**, 80–90 (2017).

## Acknowledgements

This work was supported by the NIH 4D Nucleome Program (U01 DA040601, C.P.B.), the Howard Hughes Medical Institute (C.P.B.) and the National Science Foundation, through the Center for the Physics of Biological Function (PHY-1734030) and the Graduate Research Fellowship Program (DCE-1656466, D.S.W.L.). We thank J. Riback, P. Ronceray, S. Shimobayashi, A. Strom, Y. Zhang, and the rest of the Brangwynne and Wingreen groups for constructive comments on this work. We also thank S. Keller (University of Washington, Department of Chemistry) for useful discussions at the Marine Biological Laboratory. We acknowledge E. Gatzogiannis for microscopy assistance and K. Rittenbach and the Princeton Molecular Biology Flow Cytometry Resource Facility, which is partially supported by the Cancer Institute of New Jersey Cancer Center Support Grant (P30CA072720), for assistance with cell-sorting experiments.

## Author contributions

D.S.W.L., N.S.W. and C.P.B. conceptualized the project and wrote the manuscript. D.S.W.L. performed the experiments, formal data analysis, theory and simulations.

## Competing interests

C.P.B. is a founder and consultant for Nereid Therapeutics. All other authors declare no competing interests.

## Additional information

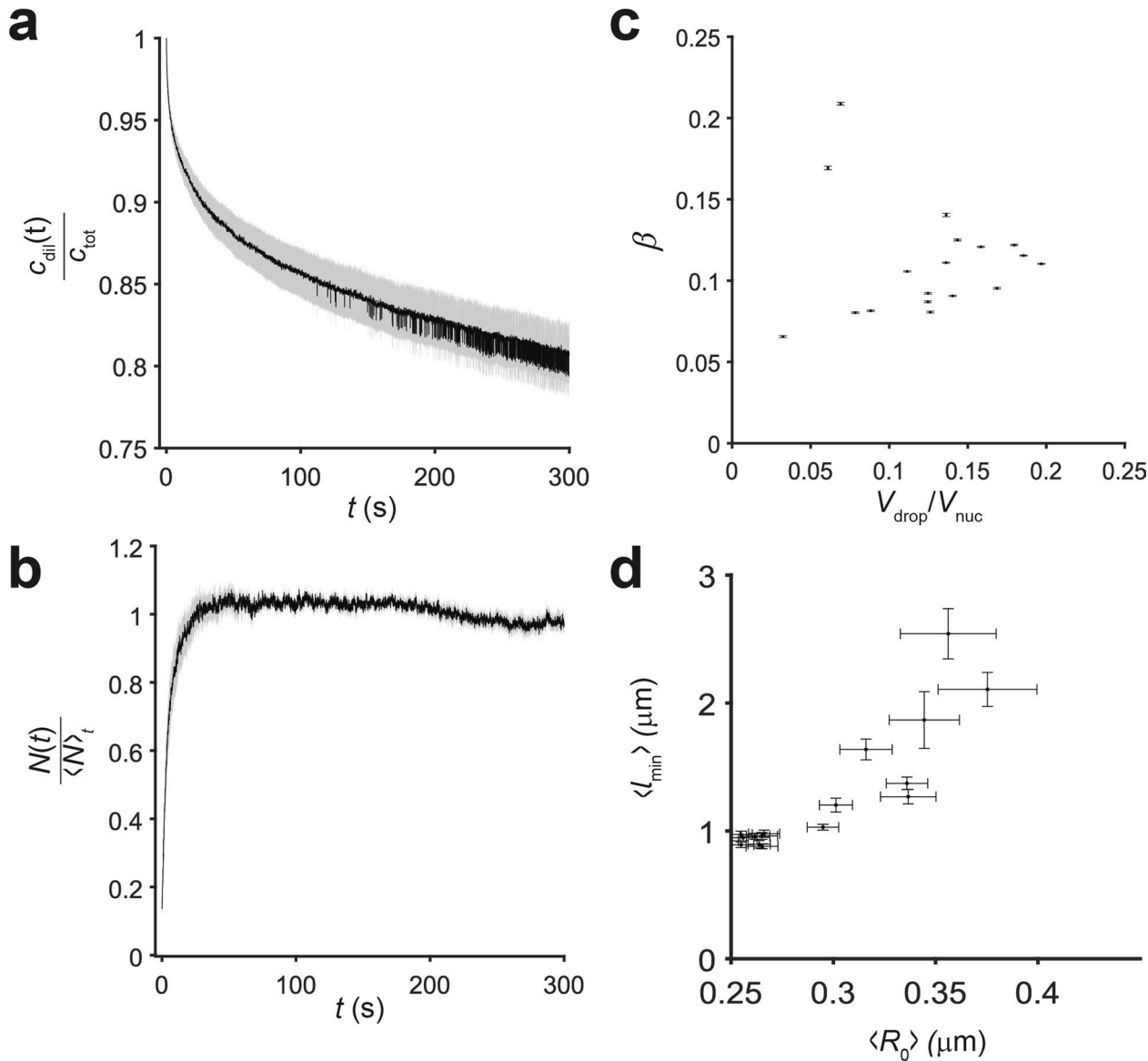
**Extended data** is available for this paper at <https://doi.org/10.1038/s41567-020-01125-8>.

**Supplementary information** is available for this paper at <https://doi.org/10.1038/s41567-020-01125-8>.

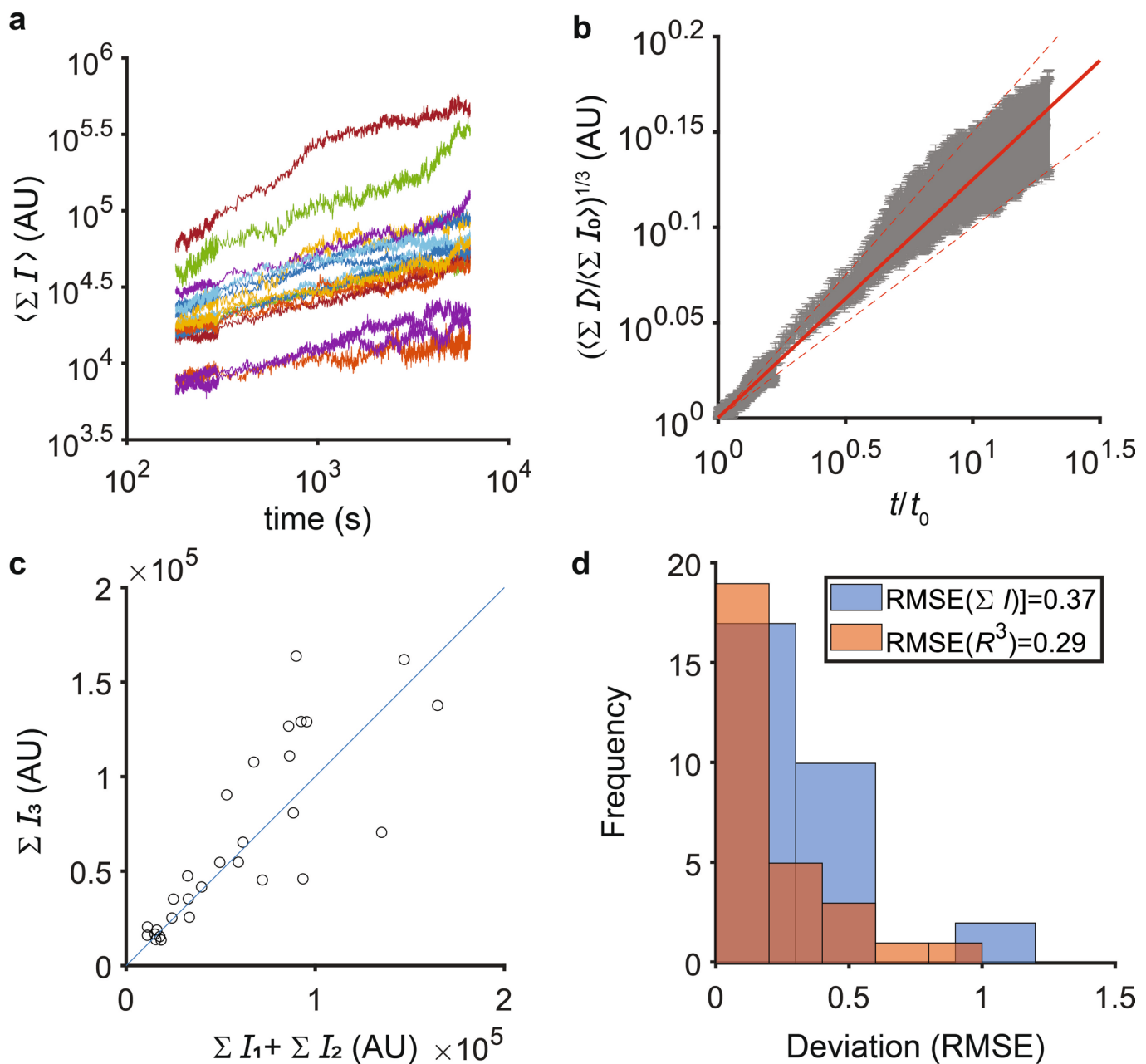
**Correspondence and requests for materials** should be addressed to N.S.W. or C.P.B.

**Peer review information** *Nature Physics* thanks David Zwicker and the other, anonymous, reviewer(s) for their contribution to the peer review of this work.

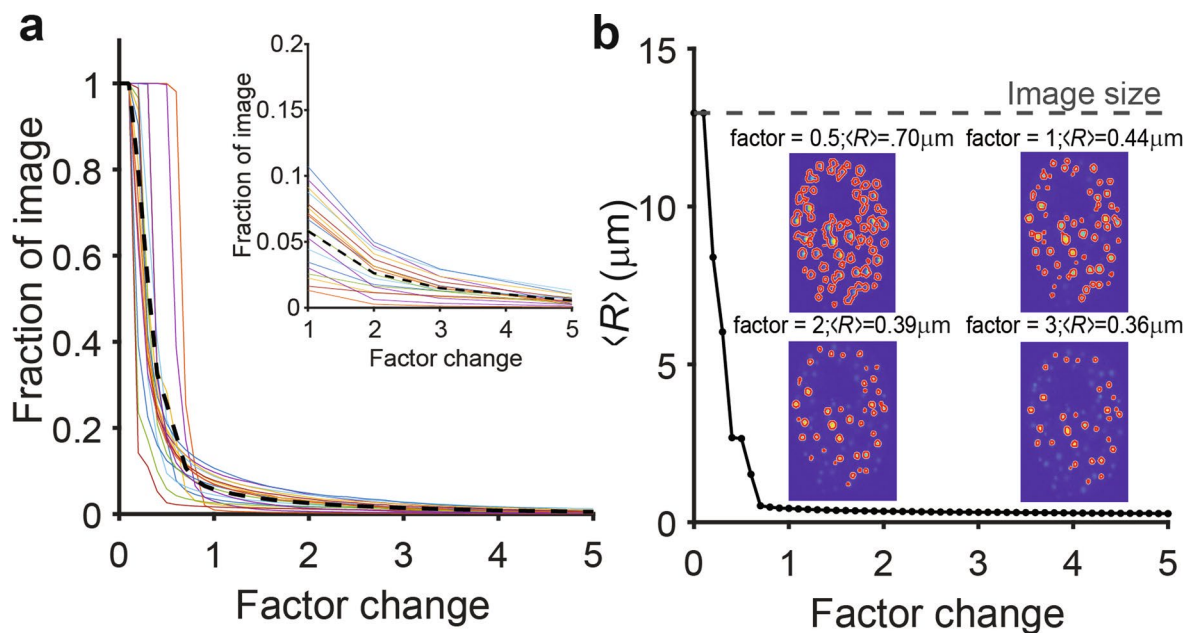
**Reprints and permissions information** is available at [www.nature.com/reprints](http://www.nature.com/reprints).



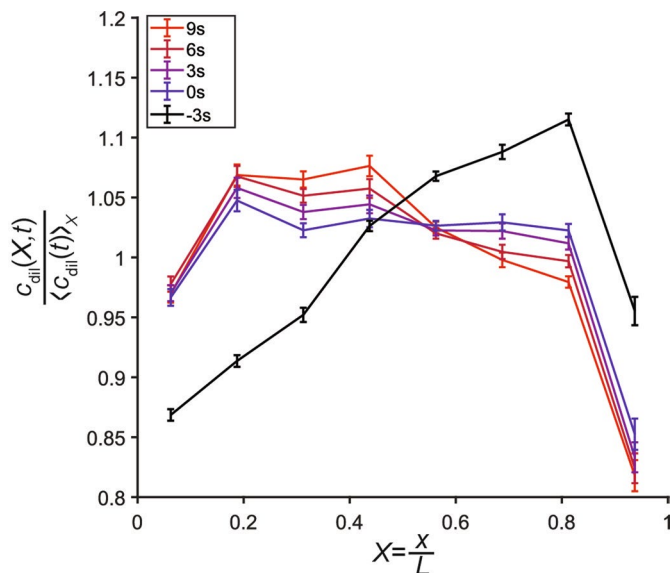
**Extended Data Fig. 1 | We characterized our system at early times immediately following a blue-light quench by taking high-speed images for the first 5 minutes of activation.** **a**, First, the degree of supersaturation was calculated by estimating the intensity in the nucleus but outside droplets and dividing by the average nuclear intensity in the first frame (that is, before any visible condensation). This ratio of intensities was averaged over cells for each timepoint; shading represents standard error of the mean. Supersaturation initially decreased very quickly following activation and continues to decrease much more slowly after 100 seconds ( $t_0$  was set to 180 s), which we attribute to photobleaching. **b**, To quantify nucleation dynamics, the number of droplets was calculated at each frame following activation: a quick increase is followed by saturation and then a slow decrease as droplets begin to coalesce. For each cell, the number of droplets was taken at each frame, divided by the time average for that cell, and then averaged over cells. Error bars reflect standard error of the mean across cells. **c**, To characterize the heterogeneity of coarsening behavior across cells, we individually fit the average droplet radius versus time for each cell to obtain a coarsening exponent. We also computed the volume fraction of droplets in each cell by dividing the number of pixels containing droplets at the final frame of activation (105 minutes) by the total number of pixels in the nucleus in the first frame of activation. The best-fit coarsening exponent for individual cells (error bar is 95% CI) was plotted against this volume fraction. The cell-to-cell variation in the coarsening exponent decreases with volume fraction, approaching an average value of ~0.12. **d**, Finally, for our estimate of the average rate of droplet growth due to subdiffusive merger, we compared minimum inter-droplet distance per droplet ( $\langle l_{\text{min}} \rangle$ ) versus average radius of droplets at  $t_0$  per cell and found that because volume fraction and nuclear size are similar over the cell population, the two quantities are strongly correlated. Error bars reflect SEM.



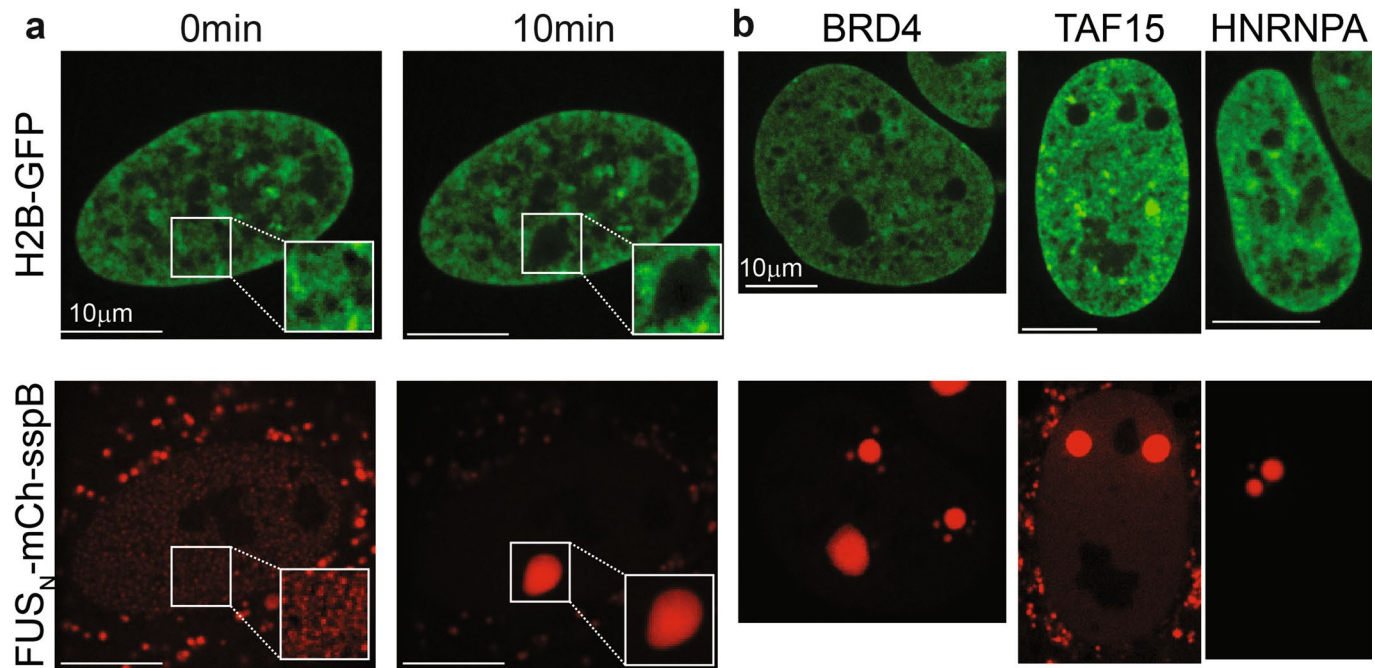
**Extended Data Fig. 2 | Analysis from Figs. 1c,d and 2d were repeated using an integrated intensity metric to estimate the size of droplets.** **a**, Average integrated droplet intensity grows as a power law in time. **b**, Nondimensionalizing with  $t_0 = 3$  min, averaging, and fitting gives a coarsening exponent of  $\beta = 0.13 \pm 0.01$  (95% CI of fit). **c**, Integrated intensity is conserved among collisions. **d**, Mean squared error (MSE) was calculated by assuming that volume must be conserved among collisions and then determining the deviation of the final volume post collision from the prediction, that is, as  $MSE = \left\langle \left(1 - \frac{V_1+V_2}{V_3}\right)^2 \right\rangle$ , where  $V_i = R_i^3$  or  $\sum I_i$  for radius and integrated intensity methods, respectively. The root mean square error (RMSE) is similar but slightly greater for the integrated intensity method.



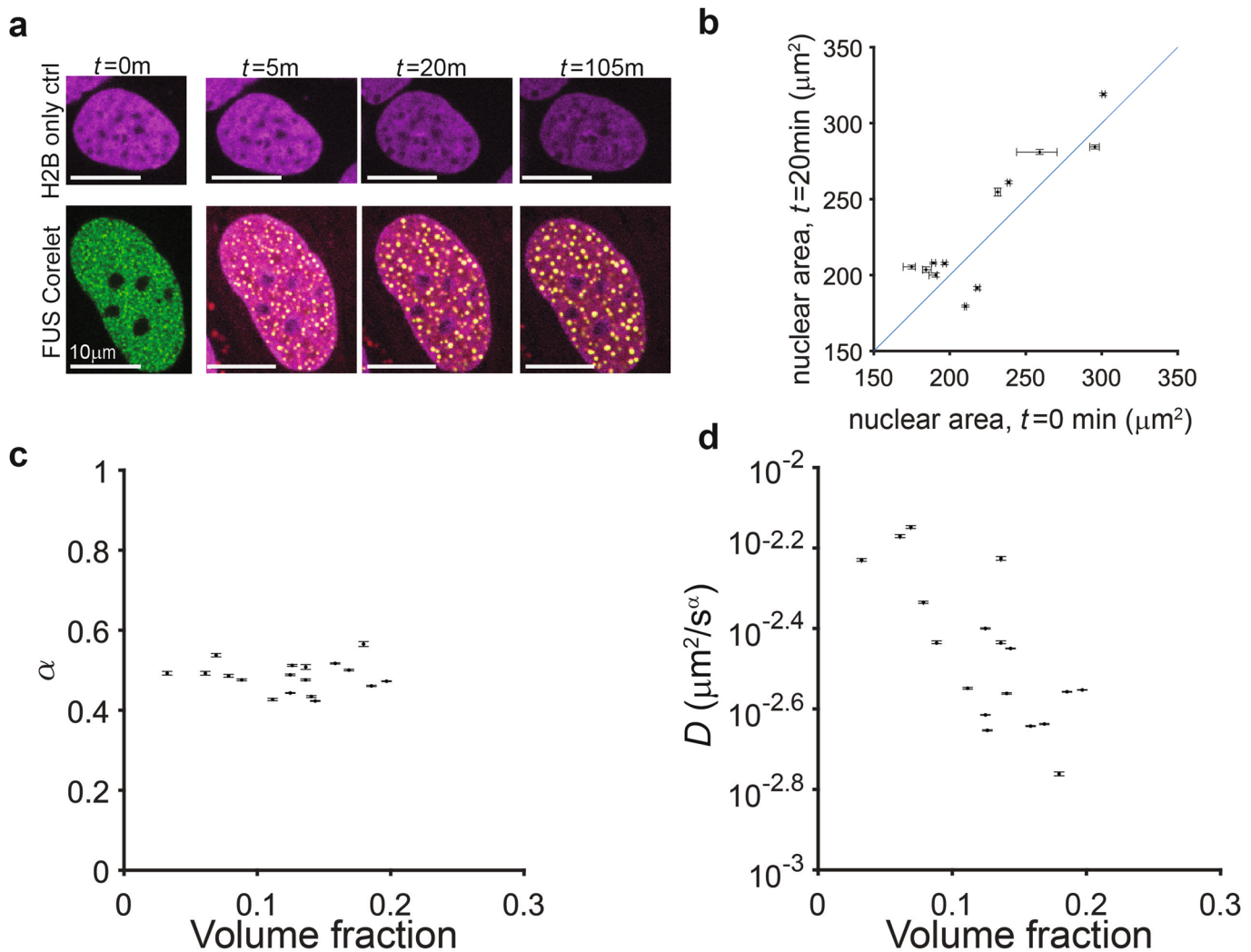
**Extended Data Fig. 3 | Average droplet size and geometry is robust to thresholding of images.** **a**, To test the robustness of the image segmentation to thresholding, we first calculated the threshold as described in the main text methods (two standard deviations above mean nuclear intensity at time 0). We then multiplied the threshold by a factor ranging from 0 to 5 ('Factor change') and calculated what percentage of each image was above the threshold and would be identified as a droplet ('Fraction of image'). Each colored curve corresponds to a single image containing one nucleus (N=18 images total) after 105 minutes of activation; black dashed line reports the average over all images. Trivially, the entire image is above the threshold at a factor value of 0 and decreases quickly. However, as the factor approaches 1 and higher values (that is, the chosen threshold) the fraction of the image segmented decreases only slowly (see inset), suggesting that segmentation is robust with respect to the threshold above these values. **b**, The identical procedure was applied to the same images to evaluate the dependence of the average droplet radius on threshold, as demonstrated in inset example images. Similar to the fraction of image metric, the average droplet radius was robust above a factor of approximately 0.75, suggesting that our results are not sensitive to the precise threshold.



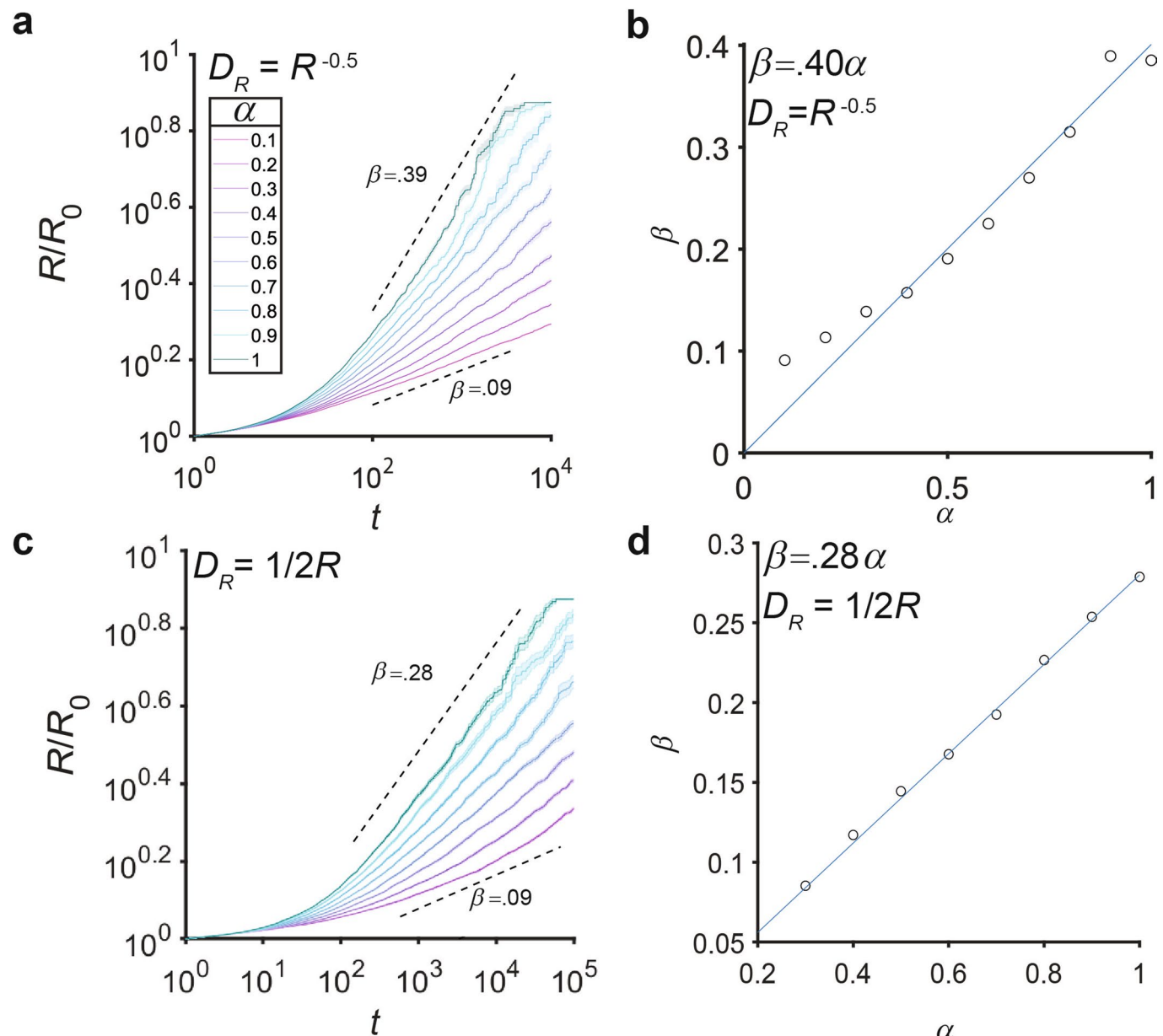
**Extended Data Fig. 4 | Equilibration of dilute-phase concentration in Fig. 2e, f is fast.** Nuclei from Fig. 2e were segmented and pixel intensity in the dilute phase was binned by location with respect to the gradient of activation, normalized, averaged over cells, and plotted. Cells were activated using a blue light intensity gradient for 30 seconds; at the end of that time, a gradient was observed in the dilute-phase concentration, favoring the side of the nucleus experiencing higher intensity stimulation (black curve). Within one frame (3 seconds) following the switch to global activation, the concentration of protein in the dilute phase became uniform (blue curve). By 6 seconds (dark red curve), small sub-diffraction-size droplets began to nucleate in the previously unactivated half of the nucleus, accounting for the slight increase in intensity which persists in the 9 second profile (red curve).



**Extended Data Fig. 5 | Example images of nuclei undergoing local activation.** **a**, Nuclei exhibit typical chromatin structure before local activation, whereupon chromatin becomes depleted in regions where droplets form. **b**, Outside of regions containing droplets (lower row), chromatin structure is unperturbed with respect to typical U2OS cells. Multiple droplets can be formed in a single nucleus given a sufficient concentration of material.



**Extended Data Fig. 6 | Cell size and morphology is minimally affected by blue light activation.** **a**, Nuclear structure and morphology in both FUS Corelet cells expressing H2B-miRFP and in a control line expressing only H2B-miRFP is qualitatively unaffected by typical imaging protocols. **b**, Nuclear size is identical before and after 20 minutes of activation, based on segmentation on pre-activated ferritin “core” (GFP) image and post-activation H2B-miRFP image, suggesting no major change in osmotic environment of the nucleus. **c**, Diffusive exponent  $\alpha$  is unaffected by volume fraction, remaining at approximately 0.5 for volume fractions ranging from 5% to 20%, suggesting that the same material properties of chromatin are measured by droplet MSDs regardless of volume fraction. **d**, Effective diffusion coefficient decreases with droplet volume fraction, consistent with data in Fig. 6 suggesting that droplet size is inversely correlated with diffusion coefficient, since cells with higher volume fractions have larger average droplet sizes.



**Extended Data Fig. 7 | Scaling behavior of coarsening simulated with  $D_R = \frac{1}{\sqrt{R}}$  and  $D_R = \frac{1}{2R}$ .** **a**, To test how the relation between  $\alpha$  and  $\beta$  changes depending on the scaling of  $D_R$  with  $R$ , step size was scaled with  $R^{-0.5}$ . As in Fig. 3, values of  $\alpha$  were chosen ranging from 0.1 to 1 with 20 replicates per condition, and droplets were merged over  $10^4$  timesteps. Average radius of droplets in each replicate was averaged for each condition over 20 replicates and plotted. Shaded error bar reflects standard error of the mean. Power laws were fit between  $10^2$  and  $5 \times 10^3$  timesteps. **b**, The best-fit coarsening exponent  $\beta$  was plotted against the input  $\alpha$  for each condition and fit with a line passing through the origin (0,0), yielding a slope of 0.40. **c**, To test whether a non-trivial number of mergers were missed in the simulation conditions in Fig. 3, simulations were repeated with halved step size (that is,  $D_R = \frac{1}{2R}$  instead of  $D_R = \frac{1}{R}$ ). The dynamics are quite similar, demonstrating increasing coarsening exponent with increasing subdiffusive exponent, suggesting that mergers are rarely missed in the original simulation. **d**, With halved step size, relation between coarsening and diffusive exponent is similar (0.28, blue reference line) to simulations in Fig. 3 (0.3), as well as to theoretical prediction (0.33).

## Reporting Summary

Nature Research wishes to improve the reproducibility of the work that we publish. This form provides structure for consistency and transparency in reporting. For further information on Nature Research policies, see our [Editorial Policies](#) and the [Editorial Policy Checklist](#).

### Statistics

For all statistical analyses, confirm that the following items are present in the figure legend, table legend, main text, or Methods section.

n/a Confirmed

- The exact sample size ( $n$ ) for each experimental group/condition, given as a discrete number and unit of measurement
- A statement on whether measurements were taken from distinct samples or whether the same sample was measured repeatedly
- The statistical test(s) used AND whether they are one- or two-sided  
*Only common tests should be described solely by name; describe more complex techniques in the Methods section.*
- A description of all covariates tested
- A description of any assumptions or corrections, such as tests of normality and adjustment for multiple comparisons
- A full description of the statistical parameters including central tendency (e.g. means) or other basic estimates (e.g. regression coefficient) AND variation (e.g. standard deviation) or associated estimates of uncertainty (e.g. confidence intervals)
- For null hypothesis testing, the test statistic (e.g.  $F$ ,  $t$ ,  $r$ ) with confidence intervals, effect sizes, degrees of freedom and  $P$  value noted  
*Give  $P$  values as exact values whenever suitable.*
- For Bayesian analysis, information on the choice of priors and Markov chain Monte Carlo settings
- For hierarchical and complex designs, identification of the appropriate level for tests and full reporting of outcomes
- Estimates of effect sizes (e.g. Cohen's  $d$ , Pearson's  $r$ ), indicating how they were calculated

*Our web collection on [statistics for biologists](#) contains articles on many of the points above.*

### Software and code

Policy information about [availability of computer code](#)

Data collection Nikon-Elements Advanced Research was used for all data collection.

Data analysis Fiji and MATLAB were used in all analysis (as detailed in manuscript); custom code available upon request.

For manuscripts utilizing custom algorithms or software that are central to the research but not yet described in published literature, software must be made available to editors and reviewers. We strongly encourage code deposition in a community repository (e.g. GitHub). See the Nature Research [guidelines for submitting code & software](#) for further information.

### Data

Policy information about [availability of data](#)

All manuscripts must include a [data availability statement](#). This statement should provide the following information, where applicable:

- Accession codes, unique identifiers, or web links for publicly available datasets
- A list of figures that have associated raw data
- A description of any restrictions on data availability

All data (microscopy images, code and analysis outputs) available upon request.

# Field-specific reporting

Please select the one below that is the best fit for your research. If you are not sure, read the appropriate sections before making your selection.

Life sciences       Behavioural & social sciences       Ecological, evolutionary & environmental sciences

For a reference copy of the document with all sections, see [nature.com/documents/nr-reporting-summary-flat.pdf](https://nature.com/documents/nr-reporting-summary-flat.pdf)

## Life sciences study design

All studies must disclose on these points even when the disclosure is negative.

Sample size	Sample size was not predetermined; replicates were performed until statistical error propagation indicated appropriate confidence.
Data exclusions	For size-dependence data, data points below diffraction limit were excluded (determined by empirical calibration using beads of known size).
Replication	Each experiment was performed in 2-3 technical replicates (i.e., parental cells were infected, imaged, and analyzed independently in each replicate).
Randomization	Randomization was not required for this study.
Blinding	Blinding was not required for this study.

## Reporting for specific materials, systems and methods

We require information from authors about some types of materials, experimental systems and methods used in many studies. Here, indicate whether each material, system or method listed is relevant to your study. If you are not sure if a list item applies to your research, read the appropriate section before selecting a response.

### Materials & experimental systems

n/a	Involved in the study
<input checked="" type="checkbox"/>	<input type="checkbox"/> Antibodies
<input type="checkbox"/>	<input checked="" type="checkbox"/> Eukaryotic cell lines
<input checked="" type="checkbox"/>	<input type="checkbox"/> Palaeontology and archaeology
<input checked="" type="checkbox"/>	<input type="checkbox"/> Animals and other organisms
<input checked="" type="checkbox"/>	<input type="checkbox"/> Human research participants
<input checked="" type="checkbox"/>	<input type="checkbox"/> Clinical data
<input checked="" type="checkbox"/>	<input type="checkbox"/> Dual use research of concern

### Methods

n/a	Involved in the study
<input checked="" type="checkbox"/>	<input type="checkbox"/> ChIP-seq
<input checked="" type="checkbox"/>	<input type="checkbox"/> Flow cytometry
<input checked="" type="checkbox"/>	<input type="checkbox"/> MRI-based neuroimaging

## Eukaryotic cell lines

Policy information about [cell lines](#)

Cell line source(s)	U2OS (Mark Groudine lab, Fred Hutchinson Cancer Research Center), 293T (LentiX from Takara Bio)
Authentication	Cell lines were not authenticated. Visual analysis of nuclear and cytoplasmic morphology matched expectations for U2OS cells.
Mycoplasma contamination	Cell lines were not tested for mycoplasma contamination. No cytoplasmic puncta were seen with Hoechst stain.
Commonly misidentified lines (See <a href="#">ICLAC</a> register)	Name any commonly misidentified cell lines used in the study and provide a rationale for their use.